PROCEEDINGS A

royalsocietypublishing.org/journal/rspa

Research

Cite this article: Cylke A, Serbanescu D, Banerjee S. 2024 Energy allocation theory for bacterial growth control in and out of steady state. *Proc. R. Soc. A* **480**: 20240219.
https://doi.org/10.1098/rspa.2024.0219

Received: 25 March 2024
Accepted: 23 August 2024

Subject Category:
Physics

Subject Areas:
cellular biophysics, biophysics, bioenergetics

Keywords:
bacterial growth, cell morphology, bacterial metabolism, metabolic rate, energy allocation, bacterial physiology

Author for correspondence:
Shiladitya Banerjee
e-mail: shiladtb@andrew.cmu.edu

Energy allocation theory for bacterial growth control in and out of steady state

Arianna Cylke[1], Diana Serbanescu[2,3] and Shiladitya Banerjee[1]

[1]Department of Physics, Carnegie Mellon University, Pittsburgh, PA 15213, USA
[2]Department of Physics and Astronomy, University College London, London WC1E 6BT, UK
[3]Institute for the Physics of Living Systems, University College London, London WC1E 6BT, UK

AC, 0000-0003-4462-2170; SB, 0000-0001-8000-2556

Efficient allocation of energy resources to key physiological functions allows living organisms to grow and thrive in diverse environments and adapt to a wide range of perturbations. To quantitatively understand how unicellular organisms utilize their energy resources in response to changes in growth environment, we introduce a theory of dynamic energy allocation that describes cellular growth dynamics by partitioning metabolizable energy into key physiological functions: growth, division, cell shape regulation, energy storage and loss through dissipation. By optimizing the energy flux for growth, we develop the equations governing the time evolution of cell morphology and growth rate in diverse environments. The resulting model accurately captures experimentally observed dependencies of bacterial cell size on growth rate, superlinear scaling of metabolic rate with cell size and predicts nutrient-dependent trade-offs between energy expended for growth, division and shape maintenance. By calibrating model parameters with experimental data for the model organism *Escherichia coli*, our model describes bacterial growth control in dynamic conditions, particularly during nutrient shifts and osmotic shocks. Integrating both the mechanical properties of the cell and underlying biochemical regulation, our model predicts the driving factors behind a wide range of observed morphological and growth phenomena with minimal added complexity.

THE ROYAL SOCIETY PUBLISHING

1. Introduction

Living organisms face the challenge of continuously investing energy to fuel growth, biomechanical activities and the maintenance of biomass. How energy uptake is allocated between the synthesis of new biomass and maintenance of existing mass to promote organism growth and reproduction is of central importance to ecology and evolution. Previous work has used energy budget models to understand ontogenetic growth in animals [1–5], where some fraction of the assimilated food is oxidized to sustain the total metabolic rate and the remaining fraction is synthesized and stored as biomass. While energy budget models have provided a quantitative and conceptual understanding of whole-organism growth in animals, how energy allocation strategies are implemented in single-celled microorganisms, remains an open question [6,7]. Here, we present a biophysical theoretical framework for dynamic allocation of cellular energy for key physiological tasks in bacteria, going beyond existing phenomenological models of microbial metabolism [8,9]. Our theory quantifies how assimilated nutrient energy is dynamically allocated for bacterial growth, division, dissipation and shape maintenance. We apply this framework to study bacterial growth and morphogenesis in steady and dynamic environments.

Much work has been done in recent years to understand how bacteria adapt their growth physiology in response to changes in nutrient environment [10]. Resource allocation models, based on coarse-grained partitioning of the cellular proteome into a few functional components, have provided a quantitative framework to predict how trade-offs between metabolic and gene expression machinery of the cell regulate bacterial growth rate [11–15]. While these theories are mostly focused on steady-state behaviours, recent studies have extended resource allocation models to describe transitions between steady states [16–20]. Despite these advances, models that only consider resource allocation of biochemical species are inadequate to describe physical behaviours of the cell, in particular how cellular resources are used for the control of cell shape, bioenergetics and mechanical activities. In addition, investigating perturbations from steady-state requires adding more proteome sectors, which can quickly complicate the model [20]. On the other hand, mechanical models of cell growth have been developed to describe cell shape dynamics in growing bacterial cells [21,22], but they do not take into account biochemical regulation and decision-making components of the cell. While each of the aforementioned models function satisfactorily within their proposed scopes, they do not capture the interplay between mechanical activity and biochemical regulation. To bridge this knowledge gap, we introduce a new theoretical framework for bacterial growth and cell shape regulation based on allocation of uptake energy for physical and biochemical processes, including growth, division, storage and shape maintenance.

Through the optimization of energy flux for growth, we deduce the governing equations for cell size, shape and division dynamics. Upon calibrating model parameters using experimental data from the steady-state growth of the model organism *Escherichia coli*, we offer insights into how cellular energy uptake is distributed among various physiological tasks under specific nutrient conditions. Our theoretical framework aligns with multiple experimental observations, yielding predictions that shed light on the underlying driving forces of these phenomena. Our findings reveal a positive correlation between cell size and growth rate as a natural outcome of energy flux optimization. Analysis of cellular metabolic rates yields a superlinear scaling relationship between metabolic rate and bacterial cell size. Furthermore, our model is adept at explaining complex transient behaviours observed in nutrient shift experiments [17], where nutrients are added or removed during growth to study responses to dynamic environments more similar to those found in nature. Fitting our model to nutrient shift data [17,23], we find that overshoots and undershoots past the final steady-state growth rate stem from disparate time-scales governing nutrient importation and changes in cell morphology. Notably, we showcase the model's flexibility in capturing the initial response to osmotic shocks [24], where a change of the osmolarity of the growth medium perturbs the water content of the cytoplasm, through manipulation of turgor pressure, highlighting its capability to predict

energy reallocation under mechanical stress. Integrating the effects of both biochemical and mechanical regulation of growth, our unified approach offers a modular framework with broad applicability across organisms, offering a new perspective on the regulation of microbial growth physiology.

2. Dynamic energy allocation theory

(a) Energy flux balance

The starting point of our theory is the condition of energy flux balance, such that the rate of uptake of food energy, E_{in}, is equal to the rate at which the consumed energy is used to fuel cellular metabolic processes (E_{met}) plus the rate at which the accumulated energy is stored in cellular biomass (E_{stored}) [5],

$$\frac{\mathrm{d}E_{\text{in}}}{\mathrm{d}t} = \frac{\mathrm{d}E_{\text{met}}}{\mathrm{d}t} + \frac{\mathrm{d}E_{\text{stored}}}{\mathrm{d}t}\,. \tag{2.1}$$

For a growing and replicating bacterial cell, we assume that the metabolic energy, E_{met}, is used for four major tasks: (i) E_{growth}, energy used for cellular growth and biosynthesis; (ii) E_{div}, energy expended for cell division; (iii) E_{mech}, mechanical energy expended for the maintenance of cell shape, structure and size; and (iv) E_{d}, the amount of energy lost due to dissipation. For simplicity, we consider a non-motile cell and neglect energy due to locomotion. This simplification is consistent with the non-motile strains of *E. coli* that we later use to calibrate the model. A schematic depicting the coarse-grained energy partitioning scheme is shown in figure 1.

The coarse-grained energy components are functions of the state variables $\{q_i(t)\}$ that represent the set of independent variables that describe the macroscopic state of the cell. For a bacterial cell, these could be defined by cellular morphological parameters as well as the abundance of proteins in a particular proteome sector. Having framed the central theoretical concept of our model, we now turn to modelling the aforementioned components of cellular energy.

(b) Modelling cellular energy components

Nutrient intake—Under the assumption that nutrient uptake occurs uniformly through the cell surface [25], the total energy available to the cell from nutrient intake, E_{in}, is taken to be proportional to the surface area S of the cell, such that $E_{\text{in}} = \varepsilon S$. Here, ε is proportional to the surface concentration of nutrients, the surface density of transporters and net energy imported per nutrient (benefit minus the cost of import). Note that, unlike the energy sectors that follow, E_{in} is a positive quantity rather than a cost. Both ε and S can be time-dependent and will depend on the bacterial species.

Stored energy—The stored energy in the cell is given by $E_{\text{stored}} = gV$, where V is the cell volume and g is the energy stored per unit volume of the biomass. E_{stored} is a coarse-grained representation of biochemical storage, including unmetabolized nutrients, amino acid precursors, metabolic by-products, ATP concentration and enzymes produced for later use. While approximating g to be a constant is sufficient to capture dynamics later in this work, there is no biological reason that g cannot change over time, e.g. as the cell depletes nutrient reserves under starvation conditions. The numerical value and the time-dependence of this parameter may differ for various bacterial species and environments.

Turgor pressure—The energy due to turgor pressure is given by $E_{\text{turgor}} = -PV$, where P is the turgor pressure and V is the cell volume.

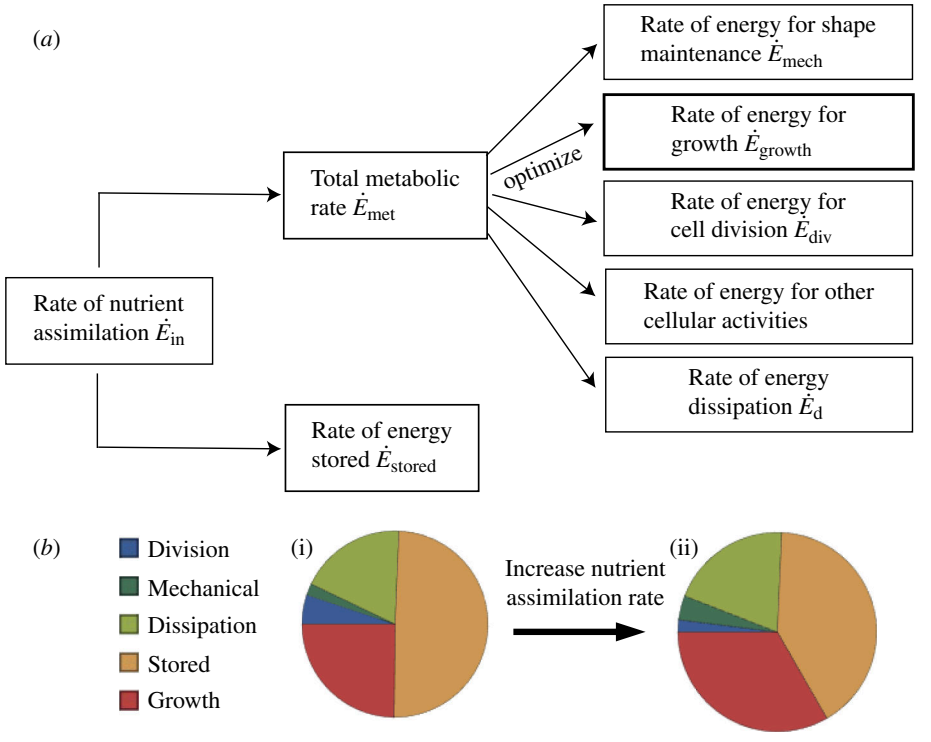

Figure 1. Dynamic energy allocation theory. (*a*) A schematic depicting how a bacterial cell partition assimilated nutrient energy into diverse cellular tasks. The energy utilized for growth, $\dot{E}_{growth}$, is highlighted to indicate that it is optimized to derive the governing equations of motion. (*b*) Energy allocation during cellular growth. The pie charts indicate fractions of assimilated energy E_{in} utilized for each energy sector at growth rate $\kappa = 0.9$ h^{-1} (i) and $\kappa = 2$ h^{-1} (ii).

Cell shape maintenance—The mechanical energy for maintaining the shape of the cell envelope, E_{mech}, is given by the sum of the strain energy in the bacterial cell envelope (E_{strain}), and the bending energy required to maintain cell curvature (E_{curv}):

$$E_{mech} = E_{curv} + E_{strain}\,. \tag{2.2}$$

For a rod-shaped bacterial cell approximated as a cylinder of length L and radius of cross-section R, the curvature energy is given by

$$E_{curv} = \kappa_c \pi R L \left(R^{-1} - R_0^{-1}\right)^2, \tag{2.3}$$

where R_0 is the preferred radius of cross section and κ_c is the bending rigidity. To compute the strain energy in the cell envelope due to turgor pressure P, we assume that the rate of cell growth is slower than mechanical relaxation, such that the cell envelope is always in mechanical equilibrium. Treating each individual peptide cross-linker as a spring with stiffness k_s, the strain energy in the peptidoglycan cell wall can be expressed as $E_{strain} = \frac{1}{2} N_g k_s \rho_p (l - l_0)^2 2\pi R$, where N_g is the number of glycan strands (with a layer of cross-linkers in-between each strand), ρ_p is the areal density of peptide cross-linkers, l is the deformed length and l_0 is the undeformed (rest) length of an individual cross-linker. Note that the cross-linkers all deform uniformly. In mechanical equilibrium, balancing the forces from the cross-linker springs and the turgor pressure yields the length deformation: $l - l_0 = PR/(2k_s\rho_p)$. As a result, we can rewrite the strain energy as:

$$E_{\text{strain}} = \rho_g L \pi \frac{P^2 R^3}{4 k_s \rho_p} = \lambda \pi R^3 L \,, \tag{2.4}$$

where $\lambda = P^2 \rho_g / 4 k_s \rho_p$ can be interpreted as the mechanical stress per unit circumference, and $\rho_g = N_g / L$ is the line density of the glycan strands (assumed to be uniform). We note that the scaling form for the strain energy in (2.4) agrees with previous calculations done using thin shell elasticity theory for a rod-shaped bacterial cell [21]. Modelling geometries other than cylindrical rods would require re-expressing these equations in terms of the appropriate geometric variables.

Cell division—Bacterial cell division relies on a large protein complex called the divisome, which orchestrates the assembly of the Z-ring around the mid-cell region [26]. The Z-ring is composed of FtsZ filaments, capable of generating constrictive bending forces [27,28]. Moreover, the divisome triggers peptidoglycan synthesis and guides the formation of the septum [29]. Previous work has demonstrated that FtsZ generates a small amount of mechanical force that is insufficient to fully constrict the mid-cell [22,30,31]. Instead, the primary driving force for cell constriction arises from cell wall synthesis at the septum [22,32,33]. Consequently, we disregard the mechanical energy cost of Z-ring constriction and model the energy of cell division as being driven by the synthesis of division proteins (e.g. FtsZ).

Defining X as the total abundance of division proteins, the energy for the synthesis of division proteins can be written as:

$$E_{\text{div}} = -\mu X \,, \tag{2.5}$$

where μ is the chemical potential for division protein synthesis. In most bacterial cells that follow the adder mechanism for cell division control [10,34], cell division is triggered once a threshold amount of division proteins is accumulated during the cell cycle [23,35–37]. Since FtsZ abundance in the Z-ring reaches a fixed threshold prior to division [36], assume that the threshold abundance of division proteins, X_0, is proportional to the cell diameter: $X_0 = 2\pi R \gamma$ [38], where γ is the proportionality constant and R is the cell radius. Therefore, the energetic cost of division during a cell cycle is $\approx -2\pi\mu\gamma R$.

Energy dissipation—Living cells can be considered as open thermodynamic systems that dissipate energy as they grow and replicate [39]. For a growing bacterial cell, the rate of energy dissipation ($\mathrm{d}E_{\mathrm{d}}/\mathrm{d}t$) is a sum of energy dissipation rate due to mechanical ($\mathcal{D}_{\text{mech}}$) and chemical components ($\mathcal{D}_{\text{chem}}$):

$$\frac{\mathrm{d}E_{\mathrm{d}}}{\mathrm{d}t} = \mathcal{D}_{\text{mech}} + \mathcal{D}_{\text{chem}}. \tag{2.6}$$

In non-equilibrium thermodynamics, a commonly made assumption is that the energy dissipation rate follows a quadratic relationship with the 'rate' of change in state variables [40–42]. The dissipation rate of mechanical energy is thus taken to be proportional to the square of the strain rate. Specifically, for a rod-shaped bacterial cell with length L and radius R, the strain rates can be expressed as $\dot{R}/R$ and $\dot{L}/L$ where the dot denotes a time derivative. Consequently, we formulate the mechanical dissipation rate as:

$$\mathcal{D}_{\text{mech}} = \frac{1}{2} V_d \left[\eta_L \left(\frac{\dot{L}}{L} \right)^2 + \eta_R \left(\frac{\dot{R}}{R} \right)^2 \right], \tag{2.7}$$

where η_L and η_R are the viscosity parameters and V_d is the volume over which dissipation occurs. We take $V_d = hS$, where h is the cell envelope thickness, and $S \approx 2\pi RL$ is the surface area of dissipation for a rod-shaped cell. Analogously, the dissipation rate of chemical variables of the system can be assumed to follow a quadratic relationship with the square of the rate of production of that chemical.

$$\mathcal{D}_{\text{chem}} = \frac{1}{2}V\left[\xi\left(\frac{\dot{X}}{V}\right)^2\right] + \text{contribution from other proteins,} \tag{2.8}$$

where ξ is a constant and the contributions from other proteins will be discussed in §2f. Therefore, the total dissipation rate due to cell envelope growth and division is:

$$\frac{\mathrm{d}E_{\mathrm{d}}}{\mathrm{d}t} = \frac{hS}{2}\left[\eta_L\left(\frac{\dot{L}}{L}\right)^2 + \eta_R\left(\frac{\dot{R}}{R}\right)^2\right] + \frac{\xi}{2V}\dot{X}^2. \tag{2.9}$$

The above form for the total dissipation rate is consistent with thermodynamic principles since the resulting dissipative forces, $-\partial\dot{E}_d/\partial\dot{q}_i$, are not symmetric under time-reversal.

Energy for growth—Cellular growth energy involves the energy required to synthesize biomass and the surface area. Here, we do not directly define the growth energy, but instead calculate it from the energy flux balance relation in equation (2.1). We can write the flux of energy used for growth as:

$$\dot{E}_{\text{growth}}(q_i, \dot{q}_i) = \dot{E}_{\text{in}} - \left(\dot{E}_{\text{div}} + \dot{E}_{\mathrm{d}} + \dot{E}_{\text{mech}} + \dot{E}'_{\text{stored}}\right), \tag{2.10}$$

where $E'_{\text{stored}} = (g - P)V$ is the effective stored energy. In exponentially growing cells, $\dot{E}_{\text{growth}}$ is proportional to the growth rate κ, which follows from the equations derived in §2d.

(c) Optimization principle

While equation (2.1) constitutes a general constraint for the cell, it is not sufficient to describe the full dynamics of $\{q_i(t)\}$. To derive the equations of motion, we impose a principle of power optimization. In particular, for a growing bacterial cell, we hypothesize that the bacterium maximizes the rate of energy (or power) utilized for growth:

$$\frac{\partial\dot{E}_{\text{growth}}}{\partial\dot{q}_i} = 0\,, \tag{2.11}$$

where dot denotes time derivative. This implies that the dynamics of the system are determined by the condition that the growth power, $\dot{E}_{\text{growth}}$, is a maximum with respect to $\dot{q}_i$, where $\dot{q}_i$ represents the rate of change in the current state $q_i(t)$.

Maximizing the rate of energy utilized for growth is similar to the maximum power principle often used in models of ecology and thermodynamics [43,44]. In the case of bacteria, the rate of energy used for growth is proportional to the growth rate of the cell. The hypothesis for maximizing the growth power is motivated by experimental observations that *E. coli* cells evolve their metabolism towards a state that maximizes growth rate [45–48]. Furthermore, previous work has shown that growth-rate maximization leads to the empirical growth laws of bacterial cells [11,12,49,50]. It is important to note that the maximum growth power hypothesis is only applicable for cells growing in medium to rich nutrient conditions. It may not be applicable for bacteria under stress, such as under starvation, when cells may prioritize maintenance over growth [51]. In addition, while differences in intra-species growth rate can be driven by the suboptimal synthesis of proteins not utilized in the current growth conditions [52], calibration of model parameters is strain-specific and the scope of our flux optimization principle does not encompass longer-term evolution.

(d) Equations governing cell growth and shape dynamics

For a rod-shaped bacterial cell such as *E. coli* or *Bacillus subtilis*, the minimal set of state variables required to describe its growth and division dynamics are the cell length L, radius R

and division protein abundance X. Thus, $q = \{L, R, X\}$. Using equation (2.11), the condition for optimizing growth power, we obtain:

$$\frac{\partial \dot{E}_{\text{growth}}}{\partial \dot{q}_i} = \frac{\partial}{\partial \dot{q}_i}\left(\dot{E}_{\text{in}} - \dot{E}'_{\text{stored}} - \dot{E}_{\text{mech}} - \dot{E}_{\text{div}} - \dot{E}_{\text{d}}\right) = 0\,. \tag{2.12}$$

Since E_{in}, E'_{stored}, E_{div} and E_{mech} are functions of q_i's only, then $\dot{E}_{\text{in}} = \sum_i (\partial E_{\text{in}}/\partial q_i)\dot{q}_i$, and similarly for the rest. Therefore, the governing equations for the dynamics of q_i are given by:

$$\frac{\partial E_{\text{in}}}{\partial q_i} = \frac{\partial E'_{\text{stored}}}{\partial q_i} + \frac{\partial E_{\text{div}}}{\partial q_i} + \frac{\partial E_{\text{mech}}}{\partial q_i} + \frac{\partial \dot{E}_{\text{d}}}{\partial \dot{q}_i}\,. \tag{2.13}$$

As a first step, by optimizing $\dot{E}_{\text{growth}}$ with respect to $\dot{X}$, we can obtain:

$$\frac{\mathrm{d}X}{\mathrm{d}t} = \frac{\mu}{\xi} V \equiv \kappa_P L\,, \tag{2.14}$$

where we defined $\kappa_P = \pi R^2 \mu/\xi$, as the rate of division protein synthesis per unit length. Equation (2.14) is identical to the model for volume-specific production of division proteins as considered previously by several authors [15,23,35–37]. Using equations (2.10) and (2.11), we derive the equations governing cell length and radius:

$$\frac{1}{L}\frac{\mathrm{d}L}{\mathrm{d}t} = \mu_L\left(2\varepsilon - g'R - \frac{U(R)}{R}\right) \equiv \kappa\,, \tag{2.15}$$

$$\frac{1}{R}\frac{\mathrm{d}R}{\mathrm{d}t} = \mu_R\left(2(\varepsilon - g'R) - \frac{\mathrm{d}U}{\mathrm{d}R}\right), \tag{2.16}$$

where $\mu_L = 1/2\eta_L h$, $\mu_R = 1/2\eta_R h$, $U(R) = E_{\text{mech}}(R, L)/\pi L$, $g' = g - P$ and κ is the longitudinal growth rate. From (2.16), we see that cells maintain a steady-state radius in a given growth condition to minimize an effective potential E_{eff} defined as:

$$E_{\text{eff}} = -\int \left(2(\varepsilon - g'R) - \frac{\mathrm{d}U}{\mathrm{d}R}\right)\mathrm{d}R = U - 2\varepsilon R + g'R^2\,. \tag{2.17}$$

With a fixed radius at steady-state, cell length increases exponentially as expected for rod-shaped bacteria. Exponential growth is contingent on sufficient energy intake (per unit surface area) ε such that $\kappa > 0$. In other words, the energy flux into the cell must surpass the mechanical energy costs and anticipated energy storage for the cell to grow. As seen in figure 2*a*, in nutrient-poor conditions, cells would need to decrease their stored energy density g (from the value we will later extract from experimental data) to permit $\kappa > 0$. Using equations (2.14)–(2.16), we can simulate the dynamics of length, radius and protein abundance over multiple generations of growth and division as shown in figure 2*b*,*c*. Division occurs once X reaches a fixed threshold, as discussed earlier. Upon changes in growth rate, induced by changes in ε, the landscape for the effective potential changes such that cells find a new radius that minimizes E_{eff} as seen in figure 2*d*.

Before constraining the model parameters from experimental data, we can obtain some general insights about the interdependence between cell size and growth. Increasing the nutrient influx ε increases the growth rate κ (2.15, figure 2*b*), as well as the division rate κ_P (figure 2*c*). As ε increases, we see that the steady-state value for cell radius R must increase to compensate (figure 2*d*). Conversely, an increase in energy storage g (while keeping ε constant) prompts a reduction in R. In simpler terms, a greater nutrient influx is associated with increased cell width, while greater energy storage is linked to decreased width. As evident from equation (2.15), the growth rate decreases with increasing mechanical energy. With an increase in either the bending stiffness κ_c or the cell envelope stress λ, cell width would decrease as the energy cost of maintaining a larger envelope is greater. Thus, without specifying the numerical values

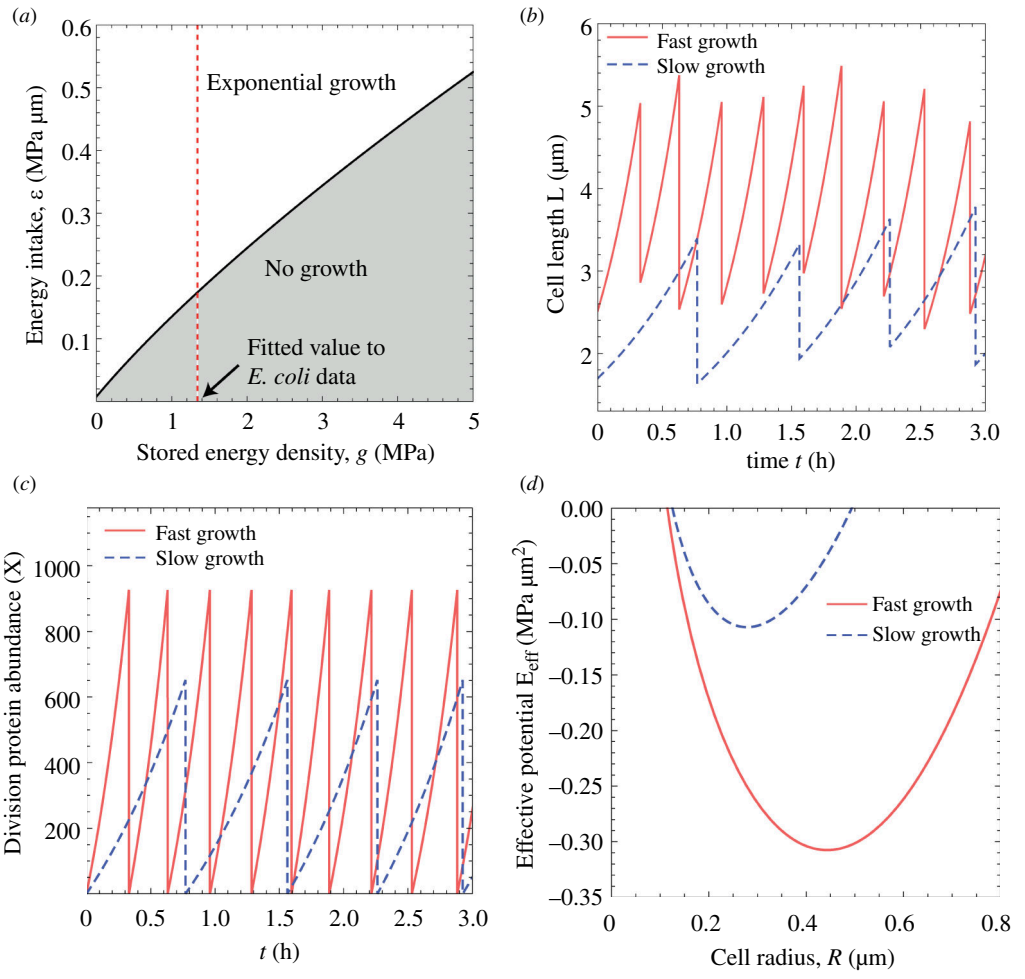

Figure 2. Single-cell growth dynamics in the energy allocation model. (*a*) Phase diagram showing regions of parameter space permitting exponential growth. The dotted red line corresponds to the value $g = 1.64$ MPa determined from experiment data, as discussed in §4. (*b*) Representative trajectories of cell length (using 2.15) for $\kappa = 0.9$ h^{-1} (blue) and $\kappa = 2$ h^{-1} (red). Noise is included in the initial size of daughter cells and cell division ratio to illustrate model stability. (*c*) Representative trajectories of division protein abundance (using 2.14) for $\kappa = 0.9$ h^{-1} (blue) and $\kappa = 2$ h^{-1} (red). (*d*) Effective potential energy landscapes (2.17) in nutrient-poor ($\kappa = 0.9$ h^{-1}, blue) and nutrient-rich environments ($\kappa = 2$ h^{-1}, red). The minimum value of each curve corresponds to the steady-state radius.

for the parameters, cell width naturally increases with the growth rate in our model, consistent with experimental data [53].

Unlike the control of cell width, the average cell length is set by the division protein accumulation threshold, X_0, and the division protein production rate, κ_P. Integrating equations (2.14), (2.15) across a cell cycle, we arrive at $\Delta L = X_0\kappa/\kappa_P$, where ΔL is the length added over a cell cycle. Thus, the added length ΔL increases with κ. ΔL also increases as X_0 increases since the cell needs to grow for longer to reach the threshold. Conversely, the increase in the production rate κ_P leads to a decrease in ΔL.

(e) Parameter determination

With the theoretical framework in place, we now turn to determining the model parameters using available experimental data on the model organism *E. coli*. All the parameters discussed in this section are listed in table 1 for ease of reference. These include mechanical, geometrical and biochemical parameters of the cell. Figure 3*a* documents our procedure of parameter determination.

Cell shape maintenance and turgor pressure—Several mechanical parameters such as the bending rigidity κ_c, cell-wall stiffness k_s and turgor pressure P can be fixed from reported measurements. From prior work, we estimate $\kappa_c = 0.03$ MPa μm^3 [30], and assume that the preferred radius of cross-section R_0 is the same as the preferred radius of curvature for MreB (200–400 nm [54]) which hold the circumferential structure of the cell wall. The parameter $\lambda = P^2\rho_g/4k_s\rho_P$ quantifies the mechanical stress on the cell envelope, which can be indirectly estimated. Prior work on thicker Gram-positive cell walls has shown that $k_s\rho_p \approx 127$ MPa [56] for each layer, of which the Gram-negative *E. coli* has only one. The turgor pressure in *E. coli* cells is $P = 0.3$ MPa [57] and $\rho_g = 1000\mu$m^{-1} [56], leading to $\lambda \approx 0.18$ MPa μm^{-1}.

Cell division—The chemical potential for division protein production can also be estimated from available data. As discussed in §2b, to minimally model cell division mechanics we consider the division protein FtsZ. Given that FtsZ contains 383 amino acids and consumes 4 ATP per added amino acid to a peptide chain [58], coupled with an energy output of 36 *kJ* per mole of ATP, we deduce $\mu = 9.2 \cdot 10^{-5}$ MPa$\cdot\,\mu$m^3/FtsZ. Furthermore, there are approximately 3200 FtsZ molecules per cell [55]. Considering that 30% of the total FtsZ is present in the ring [59], we can estimate the threshold abundance of FtsZ to be $X_0 \approx 960$. For *E. coli* cells with radius $R = 0.42\mu$m, we arrive at an approximate value of FtsZ abundance per unit circumference $\gamma \approx 364$ FtsZ μm$^{-1}\mu$.

Intake, storage and dissipation– The model comes with several other unknown parameters that may be dependent on the specific growth conditions. These include ε (energy intake per unit area), g (stored energy density), μ_L (longitudinal mobility), μ_R (radial mobility) and κ_p (division protein synthesis rate). We can determine these parameters from given experimental conditions. The first condition is that the radius measured under steady-state exponential growth [34], R^*, corresponds to the radius R that minimizes the effective potential in equation (2.17). Using this condition, we obtain the energy intake per unit area ε:

$$\varepsilon = (g - P)R^* + \frac{3}{2}\lambda R^{*2} + \frac{\kappa_c}{2}\left(\frac{1}{R_0^2} - \frac{1}{(R^*)^2}\right). \tag{2.18}$$

From experimental data on the steady-state exponential growth of bacterial cells [34], we have the second experimental condition that $L^{-1}dL/dt = \kappa_0$, where κ_0 is the nutrient-specific growth rate. Taken together with 2.15, we get:

$$\mu_L = \kappa_0\left(-\lambda R^{*2} + 2\varepsilon - (g - P)R^* - \kappa_c\left(R^{*-1} - R_0^{-1}\right)^2\right)^{-1}. \tag{2.19}$$

To find the division protein synthesis rate κ_p, we integrate equations (2.14) and (2.15) with the boundary condition that $X = X_0 = 2\pi R\gamma$ at the time of cell division. This yields,

$$\kappa_p = \frac{2\pi R\gamma}{\Delta L}\kappa. \tag{2.20}$$

Under fixed aspect ratio of *E. coli* cells [38], the above equation reduces to the condition of balanced biosynthesis $\kappa_p \propto \kappa$ [36], i.e. division protein production rate is proportional to the growth rate. Fits to experimental data for how steady-state cell radius (R^*) and newborn length

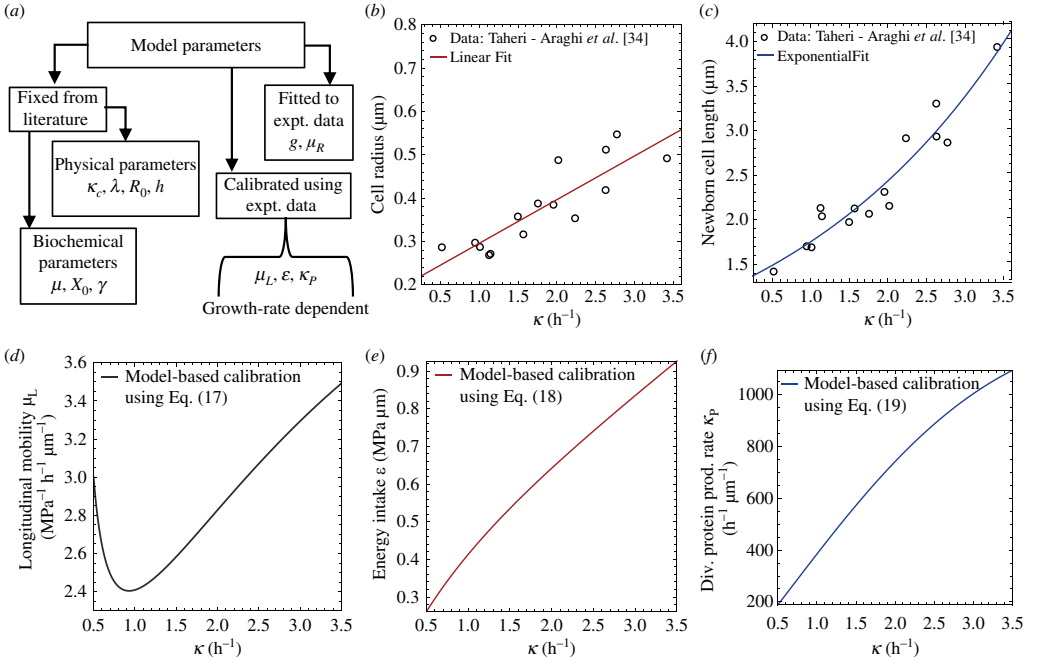

Figure 3. Calibration and inference of model parameters. (*a*) A schematic illustrating how the model parameters are determined. (*b*) Dependence of steady-state cell radius on the nutrient-specific growth rate κ for exponentially growing *E. coli* in a variety of different nutrient conditions [34]. We fit the experimental data (open circles) using a linear model $R(\kappa) = (0.1\text{h} \cdot \kappa + 0.195)\mu\text{m}$ (solid line). (*c*) Measured values of newborn cell length L_0 of exponentially growing *E. coli* in a variety of different nutrient conditions [34]. We fit the dependence of L_0 on growth rate using an exponential model $L_0(\kappa) = 1.26\mu\text{mexp}\,(\kappa \cdot 0.33\text{h})$. (*d*) Model-based inference of longitudinal mobility of the cell, μ_L, as a function of growth rate, determined using equation (2.19). (*e*) Model-based inference of energy intake per unit area, ε, as a function of growth rate, determined using equation (2.18). (*f*) Model-based inference of the division protein production rate κ_p as a function of growth rate, determined using equation (2.20).

(L_0) change with growth rate are provided in figure 3*b*,*c*, which make predictions for how the parameters μ_L, ε and κ_p change with growth rate (figure 3*d*–*f*).

Fitting parameters—The remaining two parameters μ_R (radial mobility coefficient) and g (stored energy density) are determined by fitting the model to experimental data on nutrient shifts (see §4) using a least squares algorithm comparing the experimental and simulated growth rate trajectories. μ_R controls how fast the cell radius adapts to a new steady-state value when perturbed, but it does not influence the cell morphology or energies during steady-state exponential growth. The value of μ_R depends on the type of perturbation, as seen later in §§4 and 5. While g also does not affect steady-state dynamics, it does affect the steady-state values of E_{stored}, and E_{growth}. In §4, we discuss how g is extracted from nutrient downshift data. Note that, unlike μ_R, g does not change with κ and thus does not depend on the nutrient-specific growth rate.

(f) Scope of the model

Before discussing energy allocation principles and growth dynamics, we briefly discuss the scope of our model and what we have not included explicitly in the model. A reader familiar with cell division may note that FtsZ is not the only protein required for cell division. A more complete representation of the energy put towards cell division would require estimating the

Table 1. List of model parameters.

parameter	value	physical meaning	source
κ_0	varied	steady-state growth rate	initial condition
R_0	0.3μm	MreB radius of curvature	[54]
κ_c	0.03 MPa μm^3	bending rigidity	[22]
$k_s\rho_p$	127 MPa	peptide crosslinker stiffness	[55]
P	0.3 MPa	turgor pressure	[22]
ρ_g		glycan line density	[56]
h	$5 \cdot 10^{-3}\mu$m	envelope thickness	[22]
γ	364 FtsZ μm^{-1}	division protein threshold/length	[55]
R^*	(0.1h $\kappa_0 + 0.195)\mu$m	steady-state radius	[34]
L_0	1.26exp (0.33h k_0 μm)	newborn length	[34]
μ	$9.2 \cdot 10^{-5}$ MPa μm^3	division protein chem. potential	estimated
λ	0.18 MPa /μm^3	envelope stress	derived
η_L	$1/2h\mu_L$	viscosity (length)	definition
η_R	$1/2h\mu_R$	viscosity (radial)	definition
V_d	h S	dissipation volume	definition
ξ	μ/κ_p	dissipation rate for protein production	derived
κ_p	(2.20)	division protein production rate	initial condition
μ_L	(2.19)	longitudinal mobility	initial condition
ε	(2.18)	average energy import	initial condition
μ_R	[10^{-1}, 10^2] (MPa h μm^{-}1)	radial mobility coefficient	fit
g	1.64 MPa	stored energy density	fit

synthesis cost (as discussed in §2e) for the entire divisome, as well as those associated with DNA replication and maintenance metabolism that do not contribute directly towards cell growth. Instead, what we depict here is a minimal model capable of capturing cell size control through division. Crucially, we see that the dynamics resulting from growth flux optimization for division proteins (2.14) is simply balanced biosynthesis [36], i.e. constant concentrations for optimal exponential growth. The chosen example of FtsZ is illustrative of the behaviour of all steady-state protein production; the other division proteins not mentioned explicitly likewise adhere to balanced biosynthesis. While our numerical estimate is only for one type of protein, capturing additional proteins does not change the qualitative trend of relative energy allocation decreasing with growth rate, as depicted in figure 4*b*.

Similarly, the scope of our condition-dependent determination of intake energy (§2e) is not the entire capacity of cellular metabolism. This is because equation (2.18) is only sensitive to energy sectors that influence cell morphology (i.e. L and R). For a more comprehensive picture, we can define the cost of whole-cell biosynthesis as $E_{\text{other}} = -\sum_i \mu_i X_i$, where μ_i is the chemical potential for synthesizing protein X_i. Thus, the energy flux balance can be written as:

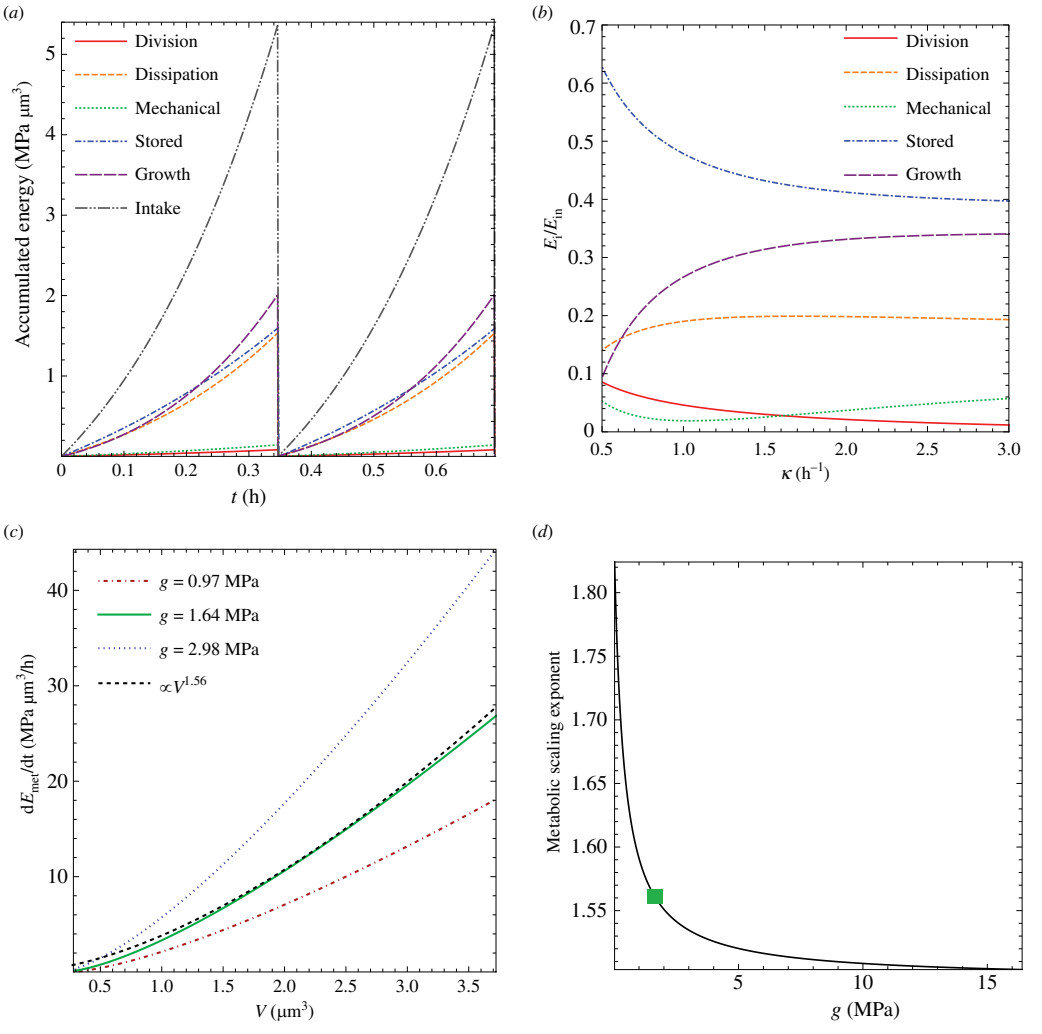

Figure 4. Energy allocation trade-offs and metabolic scaling law. (*a*) Accumulated energy since birth as a function of time, through two cycles of growth at $\kappa = 2$ h^{-1}. The intake energy (black line) is split among the various energy sectors, all of which grow at a rate proportional to the L. (*b*) Energy in each sector, E_i, normalized by the total intake energy, as a function of growth rate. E_{growth} is calculated by subtracting all other energy sectors from E_{in}. (*c*) Metabolic rate as a function of cell volume, as defined in equation (2.1). Three curves are shown for different values of the stored energy density g, with the green curve ($g = 1.64$ MPa) representing the scaling law observed experimentally (see §4). The scaling exponent is fit to be approximately 1.56 for the experimentally determined value of g. Smaller values of g (red line) have a lower scaling exponent while larger g (blue line) results in higher scaling exponents. (*d*)Metabolic scaling exponent as a function of g. The scaling exponent 1.56 for the calibrated value of $g = 1.64$ MPa is marked with a solid green square.

$$\dot{E}^*_{\text{in}} = \dot{E}_{\text{growth}} + \dot{E}_{\text{div}} + \dot{E}_{\text{d}} + \dot{E}_{\text{mech}} + \dot{E}'_{\text{stored}} + \dot{E}_{\text{other}}, \tag{2.21}$$

where $\dot{E}^*_{\text{in}}$ can be interpreted as the complete intake energy of the cell, which is related to E_{in} as $\dot{E}_{\text{in}} = \dot{E}^*_{\text{in}} - \dot{E}_{\text{other}}$. As a result, both the growth energy (2.10) and the equations of motion resulting from equation (2.11) remain unchanged.

Recent studies have incorporated aspects of energy flux modelling into proteome allocation frameworks, allowing for a more detailed modelling of cellular metabolism [6] and phenotype variability [7]. Explicitly modelling additional proteins of interest from E_{other} could extend our minimal model to make predictions about such features of cell growth at the cost of tractability.

While our model is calibrated on cells grown in various nutrient conditions, dependence of cell morphology on growth rate differs when growth rate is controlled by modulating useless protein expression [60]. Increasing useless protein expression would correspond to increasing $\dot{E}_{\mathrm{other}}$ (as these proteins would not be contributing to growth). For a fixed intake energy $\dot{E}^{*}_{\mathrm{in}}$, this would lead to a decrease in $\dot{E}_{\mathrm{growth}}$ and the resulting growth rate as expected. Furthermore, holding the total amount of intake energy, $\dot{E}^{*}_{\mathrm{in}}$, fixed while increasing $\dot{E}_{\mathrm{other}}$ would result in decreasing the intake energy available for growth processes, $\dot{E}_{\mathrm{in}}$. This would in turn be expected to decrease the radius as seen in equation (2.16) by decreasing ϵ. Given that overexpression of useless proteins increases cell size by increasing cell length at birth/division [61], our model predicts that the surface-to-volume ratio would decrease in these conditions.

3. Energy allocation strategies and metabolic scaling law

(a) Trade-offs in energy allocation

After determining the model parameters in various growth conditions, we employ the model to predict the evolution of cellular energies throughout the cell cycle and their dependence on growth rate. As cells elongate, energy in each sector accumulates in proportion to cell size (refer to §2b and §2d for definitions). Consequently, the energy of each sector $E_i(t)$ increases over the course of the cell cycle (figure 4*a*) and is then split equally among the daughter cells at division. The rate at which energy accumulates in each sector, $\dot{E}_i$, is directly proportional to L, as the energies themselves are proportional to L, thereby ensuring that the allocation to different sectors remains independent of the cell cycle. In other words, our model predicts no shifts in energy densities ($E_i(t)/L(t)$) in exponentially growing cells at steady-state.

In terms of the absolute values, all energies increase as a function of growth rate κ, since cell length and radius both increase with κ. However, normalizing cell-cycle averaged accumulated energy by the intake energy is more insightful, as it indicates how intake energy is allocated in different sectors (figure 4*b*). We thus define energy fractions relative to the intake energy as:

$$\mathcal{E}_i = \frac{\int_0^{\tau} \mathrm{d}t E_i(t)}{\int_0^{\tau} \mathrm{d}t E_{\mathrm{in}}(t)}, \tag{3.1}$$

where $i \in$ {'growth', 'stored', 'mech','div','d'} and τ is the cell cycle duration. As κ increases, we see a minimum of $\mathcal{E}_{\mathrm{mech}}$ at growth rate for cell radius $R = R_0$, with greater energy costs the further the cell deviates from that optimum growth rate (figure 4*b*). $\mathcal{E}_{\mathrm{div}}$ decreases with growth rate, as $E_{\mathrm{div}}/E_{\mathrm{in}}$ decreases with cell size ($\propto 1/V$, figure 4*b*). Notably, cells waste more energy through dissipation ($\mathcal{E}_{\mathrm{d}}$) during faster growth, given the nonlinear scaling of E_{d} with cell size. The dissipation fraction predicts that the growth efficiency of *E. coli*, $1 - \mathcal{E}_{\mathrm{d}}$, ranges from around 85% at slower growth conditions to around 81% in fast growing conditions. One of the more drastic changes is a decrease in $\mathcal{E}_{\mathrm{stored}}$ with growth rate (figure 4*b*), as cells utilize a greater fraction of the overall intake energy during fast growth conditions. Together, the changes in these sectors result in an increase in the growth energy fraction, $\mathcal{E}_{\mathrm{growth}}$, when cells are exposed to more optimal growth conditions. These predicted changes in energy fractions with growth rate are reminiscent of changes in proteome fractions with growth rate [11,12,62,63]. While the quantitative relation between proteome mass fractions and energy fractions is not yet established, the proteome fraction of the proteins regulating cell growth, such as ribosomal proteins, increases and then saturates with growth rate [63] similar to how the energy fraction allocated to growth changes with growth rate.

(b) Scaling of metabolic rate with cell size

The scaling of metabolic rate with organism size represents a fundamental characteristic trait of living organisms. It has been shown previously that the metabolic rate of birds and mammals follows a scaling law of three-fourth power relative to body size [64]. By contrast, microorganisms like bacteria display superlinear scaling of metabolic rate with cell size [65]. The biophysical origin of this superlinear scaling remains a mystery and to date, there is no mechanistic model explaining this scaling relation. Our theory now enables us to directly compute the metabolic rate, $\dot{E}_{\mathrm{met}}$, and investigate its scaling relations with cell size under various parameter values. Crucially, as elaborated below, our findings indicate that the superlinear scaling of metabolic rate with cell size naturally emerges from the increase in bacterial cell size with growth rate.

Using the equation for metabolic rate as defined in equation (2.1), and substituting our expressions for E_{in} and E_{stored}, we have:

$$\frac{\mathrm{d}E_{\mathrm{met}}}{\mathrm{d}t} = \kappa V[2\varepsilon/R - (g - P)]. \tag{3.2}$$

If ε and g were both independent of growth rate, one might expect the metabolic rate to decrease with cell size, since the positive term scales like R^{-1}. However, ε is growth rate-dependent and thus increases with cell size. Substituting the expression for ε in equation (2.18) into equation (3.2), we get:

$$\frac{\mathrm{d}E_{\mathrm{met}}}{\mathrm{d}t} = \kappa V\left[g - P + 3\lambda R + \kappa_c\left(\frac{1}{R^2 R_0} - \frac{1}{R^3}\right)\right]. \tag{3.3}$$

Using this expression, we see that the metabolic rate scales approximately as a power of cell volume (figure 4*c*). Since $V(\kappa)$ is concave (as $L(\kappa)$ is exponential, figure 3*b–c*), $\kappa(V)$ is sublinear and contributes to the overall superlinear scaling. Conceptually, the parameter g plays a role in determining this scaling as it controls both E_{stored} and ε (see equation 2.18). As shown in figure 4*d*, smaller values of g correspond to higher scaling exponents and larger values of g correspond to smaller scaling exponents. In other words, a greater amount of energy stored in the cellular biomass naturally corresponds to a lower metabolic rate. Analytically, we see that if g dominates equation (3.3), then the scaling exponent is less influenced by the terms that have R dependence. At $R = R_0$, the g, λ, κ_c terms in (3.3) are approximately 1.64, 0.16 and 0 MPa, respectively. Even when R deviates from R_0, we see that g is an order of magnitude larger than the second largest term.

Regardless of the parameter choices, our model always predicts superlinear scaling of metabolic rate with cell size for bacteria. This is in contrast to animals [5] and other microorganisms [65], which typically exhibit sublinear scaling. The key distinction that sets bacteria apart is that growth rate increases with cell size. Independence of growth rate and cell size would result in nearly linear scaling as g dominates the terms (3.3), whereas a decreasing cell size with growth rate would instead result in sublinear scaling of metabolic rate with cell size.

Recent experimental findings have indicated that populations of *E. coli* can exhibit sublinear metabolic rate scaling during long-term evolution experiments [66]. Our model does not account for inter-cellular interactions within the community (e.g. crowding and nutrient access), as well the limitation of the DNA-to-protein ratio. In other words, as cell becomes larger in these evolution experiments, the amount of DNA per cell does not change, which is not captured in our model. In addition, as mentioned in §2c, our optimization principle captures changes in phenotype rather than genotype. Our superlinear-scaling prediction is a natural consequence of exponential growth and applicable to bacteria in general, as seen in the aforementioned inter-species scaling [65], with the exact scaling exponent tuned by model parameters.

4. Dynamic response to nutrient shifts

With an understanding of cellular energy allocation strategies during steady-state exponential growth, we turn to modelling cellular response to perturbations about steady-state. To this end, we first inquired whether our model is capable of predicting growth rate dynamics in response to rapid shifts in nutrient quality in the growth medium. The change in nutrient quality can be simulated by dynamically changing the parameters ε (2.18) and μ_L (2.19), since they are dependent on the nutrient-specific growth rate (see figure 3*d*,*e*). As a simple way to represent a gradual time-dependent response, we model nutrient-induced changes in ε and μ_L as logistic functions,

$$\varepsilon(t) = \varepsilon_i + \frac{\varepsilon_f - \varepsilon_i}{1 + e^{-\theta(t - t_0)}} \tag{4.1a}$$

$$\mu_L(t) = \mu_{L,i} + \frac{\mu_{L,f} - \mu_{L,i}}{1 + e^{-\theta(t - t_0)}}, \tag{4.1b}$$

where the subscript i corresponds to the initial value of the parameter and f corresponds to the final value, θ is the steepness of the function and t_0 is the time when the shift is applied. As indicated in equations (2.15) and (2.16), the changes in ε and μ_L gradually bring the growth rate and cell size to the new steady state. The parameter μ_R introduced in equation (2.16) governs the rate at which the cell radius reaches the new equilibrium value after the shift, while the undetermined parameter g controls the timescale over which the growth rate attains the new steady-state value. Consequently, for a given nutrient shift, we have a total of four undetermined parameters: θ, t_0, μ_R and g, all of which are determined through fitting the model predictions for the growth rate to experimental data [17].

Figures 5 and 6 show the model predictions for cell size and growth rate dynamics during nutrient upshifts and downshifts, respectively. The model is fitted to experimental data from Erickson *et al*. [17], and the comparisons for growth rate dynamics during nutrient upshift and downshift are presented in figures 5*a* and 6*a*, with corresponding predictions for cell radius $R(t)$ and energy intake $\varepsilon(t)$ shown in figures 5*b* and 6*b*. During nutrient upshift, the growth rate changes gradually (figure 5*a*), and $R(t)$ closely follows the trajectory of $\varepsilon(t)$ (figure 5*b*). By contrast, during a nutrient downshift, the growth rate initially decreases sharply, undershoots the new steady-state, and gradually rebounds to a new steady-state (figure 6*a*). Unlike the upshift, $\varepsilon(t)$ quickly adjusts to its new value, while R takes hours to reach the new steady-state (figure 5*b*). Our model suggests that the difference between upshift and downshift dynamics is influenced by the timescale at which nutrient import (ε) stabilizes to the new steady-state and whether or not there is a lag between ε and cell radius R. In a nutrient downshift, nutrient removal (ε) occurs much faster than growth, resulting in a temporal lag between ε and R (figure 6*b*). Conversely, during an upshift, while the new nutrients become available externally at a similar timescale to the downshift, cells may need to upregulate nutrient import and protein synthesis to fully utilize their richer environment. These processes are inherently connected to cell growth and cell envelope synthesis, leading to no observed lag in ε and R (figure 5*b*).

To examine how changes in model parameters impact the response to nutrient shifts, we simulated single nutrient upshifts and downshifts with varying values of μ_R (figures 5*c* and 6*c*) and g (figures 5*d* and 6*d*). In upshift simulations, reducing μ_R from the fitted value introduces a lag between $\varepsilon(t)$ and $R(t)$, causing $\varepsilon(t)$ to reach the new steady-state value before $R(t)$. This results in a trajectory with an overshoot in growth rate and an increased time needed to settle into the new steady-state (figure 5*c*). Similarly, decreasing g from the fitted value also leads to a growth rate overshoot (figure 5*d*), while increasing g does not qualitatively alter the growth rate trajectory and is essentially equivalent to delaying the time of the upshift. We note that growth rate overshoots have been reported recently in microfluidic nutrient upshift experiments [23].

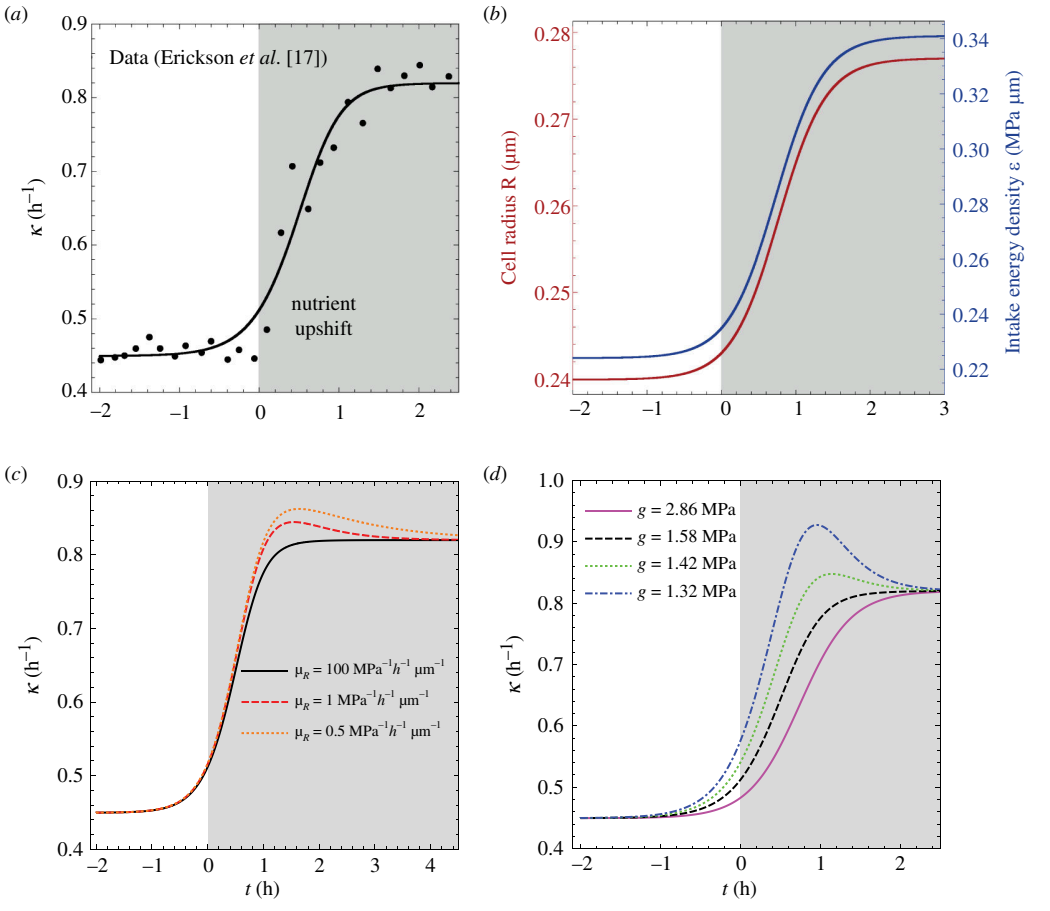

Figure 5. Modelling response to nutrient upshifts. (*a*) Growth rate versus time for a representative nutrient upshift experiment, with the experimental data shown in black solid circles and model fit shown by the solid black line. The sample experimental data, taken from Erickson *et al*. [17], are for the *E. coli* strain NCM3722, grown in 20 mM succinate with a co-utilized substrate of 0.2% glucose added/removed at $t = 0$ for the upshift/downshift. Growth rate κ is calculated by integrating equation (2.15). The fitting parameters are $\theta = 3.1$ h^{-1}, $\mu_R = 100$ MPa^{-1}h$^{-1}\mu$m^{-1} and $g = 1.64$ MPa. The white background indicates pre-shift and the grey region indicates post-shift environment. (*b*) Predicted trajectory of cell radius R, and energy intake per unit area, ε, as functions of time for the data shown in panel (*a*). (*c*) Predicted growth rate dynamics during nutrient upshift for different values of μ_R. (*d*) Predicted growth rate dynamics during nutrient upshift for different values of g.

In nutrient downshift simulations, increasing (decreasing) μ_R decreases (increases) the time required for the growth rate to attain the new steady state, without altering the amplitude of the undershoot (figure 6*c*). Conversely, smaller values of g result in a more pronounced undershoot in the growth rate, while the time to reach the new steady state remains unaffected (figure 6*d*). We observe that g is the sole parameter governing the depth of the growth rate undershoot in response to nutrient downshifts, enabling us to deduce its value through model fitting to data. Utilizing multiple nutrient downshift datasets from Erickson *et al*. [17], we do not observe a dependence of the fitted value of g on the initial and final growth rates. Fitting three datasets yields $g = 1.58$, $g = 1.61$ and 1.73 MPa, which are not correlated with the magnitude of the downshift or initial growth rate in the available data. This is not unexpected as g is a stored energy density rather than the absolute stored energy, which is influenced by initial and final growth rate-dependent cell size. Consequently, we used the average fitted value of g (≈ 1.64 MPa) for the majority of simulations in this paper.

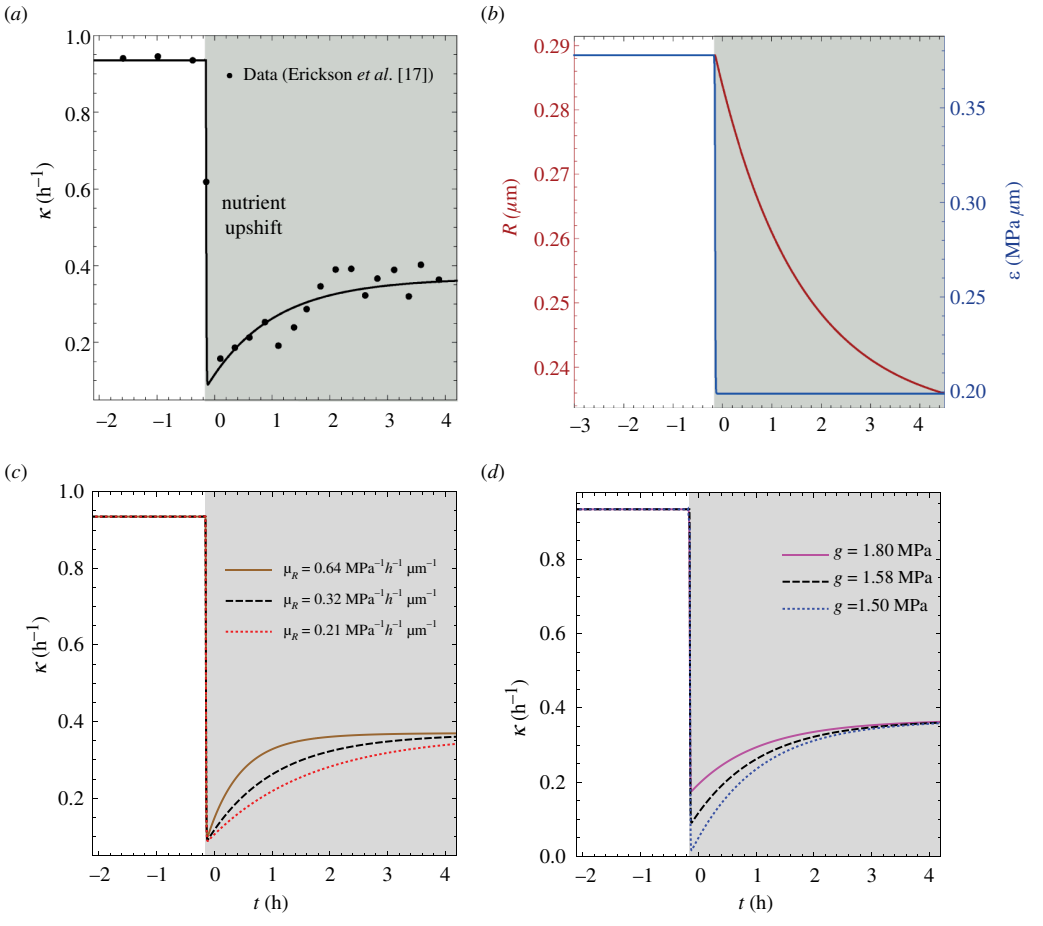

Figure 6. Modelling response to nutrient downshifts. (*a*) Growth rate versus time for a representative nutrient downshift experiment, with the experimental data shown in black solid circles and model fit shown by the solid black line. The fitting parameters are $\theta \approx 10^5$ h−1 (effectively a step function in ε), $\mu_R = 0.32$ MPa−1h−1μm−1 and $g = 1.58$ MPa. (*b*) Predicted time evolution of R and ε for the nutrient downshift data shown in panel (*a*). (*c*) Predicted growth rate dynamics during nutrient upshift for different values of μ_R. (*d*) Predicted growth rate dynamics during nutrient upshift for different values of g.

As growth rate and cell size change in response to a nutrient upshift, the cell's energy allocation strategies follow the anticipated growth rate dependencies, as shown in figure 4. However, this pattern does not hold for a downshift due to the disparate adaptation timescales of R and ε. The ε dependence is solely present in E_{in}, resulting in a rapid reduction in intake energy at $t = 0$, while the other energy sectors remain unaffected as R has not yet changed. Consequently, E_{div}, E_{mech}, E_{stored} and E_{d} temporarily account for a larger fraction of E_{in}. As a result, there is a diminished fraction of E_{in} available for growth compared with the steady-state scenario, leading to the observed undershoot.

5. Adaptation to osmotic shocks

An advantage of the energy allocation theory is that it provides a unified framework to study both mechanical and biochemical perturbations. Here, we employ the model equations to study

cellular growth response to osmotic shocks. Hyperosmotic shocks, characterized by increases in external osmolarity, result in an immediate reduction in cytoplasmic water content, leading to a decrease in growth rate and eventual plasmolysis for sufficiently prolonged shocks [24]. Conversely, hypoosmotic shocks, involving a decrease in external osmolarity, lead to an immediate increase in cytoplasmic water content and subsequent adaptation, with cells ultimately relaxing their growth rate to a sustainable value closer to the prior steady-state [24,67]. Changes in external osmolarity directly impact the turgor pressure term in the energy function, consequently changing the strain energy E_{strain} and the resulting equations of motion. Therefore, given that pressure changes initially occur on a timescale shorter than cell growth, we begin by examining the effects of rapid changes in turgor pressure on cellular growth and shape.

(a) Hyperosmotic shocks

We first consider the case of a hyperosmotic shock, which is modelled as a step-function decrease in turgor pressure from its initial value P_0 to a final value P_f (figure 7*a*). This results in a sharp decline in the growth rate, followed by a gradual recovery to a new steady-state value below the pre-shock level (figure 7*b*). The extent of recovery depends on the shock magnitude; if the shock is mild, the growth rate fully returns to the pre-shock value (figure 7*a,b*). The reduced pressure also drives a gradual reduction in cell size, with both cell length and radius decreasing to a new steady-state value post-shock (figure 7*c,d*). The reduction in cell radius facilitates growth rate recovery over time, given the negative feedback between κ and R as evident from equation (2.15). Moreover, the decreased radius reduces the length increment during the cell cycle, as the threshold amount of division proteins X_0 is proportional to the cell radius. However, this reduced cell radius contradicts experimental data [68], where it is observed that the cell radius eventually returns to its pre-shock value. Additionally, the growth rate is observed to return to its pre-shock value even for substantial shock magnitudes [24].

To capture turgor pressure and cell shape recovery post-hyperosmotic shocks, we examined a model of osmoregulation where turgor pressure relaxes back to its steady-state value P_0 according to the equation:

$$\frac{\mathrm{d}P}{\mathrm{d}t} = -\frac{1}{\tau_p}(P - P_0)\,, \tag{5.1}$$

where τ_p is the time constant for relaxation. This model draws inspiration from the fact that bacterial cells possess a diverse set of osmoregulatory proteins that regulate turgor pressure homeostasis [69]. If cells undergo osmoregulation during the adaptation to osmotic shocks [70], both the radius and growth rate recover to their respective pre-shock values as P returns to P_0. Additionally, if the timescale of radius changes (determined by μ_R^{-1}) is sufficiently larger than the timescale of osmoregulation, the period during which pressure has recovered but radius has not corresponded to an overshoot in growth rate (figure 7*b*), consistent with experimental observations [24]. Our model thus predicts that the overcorrection in growth rate following hyperosmotic shocks is a result of the mismatched timescales of pressure and morphological changes.

(b) Hypoosmotic shocks

In the case of hypoosmotic shocks, while small step function increases in pressure cause increases in growth rate (figure 8*a–d*), there is no growth rate recovery as is seen for hyperosmotic shocks. On the other hand, large pressure perturbations yield unexpected effects: cells initially shrink rather than swell and can reach new steady-state growth rates that are negative. This arises from the dominance of the P^2 term in strain energy over the turgor pressure energy

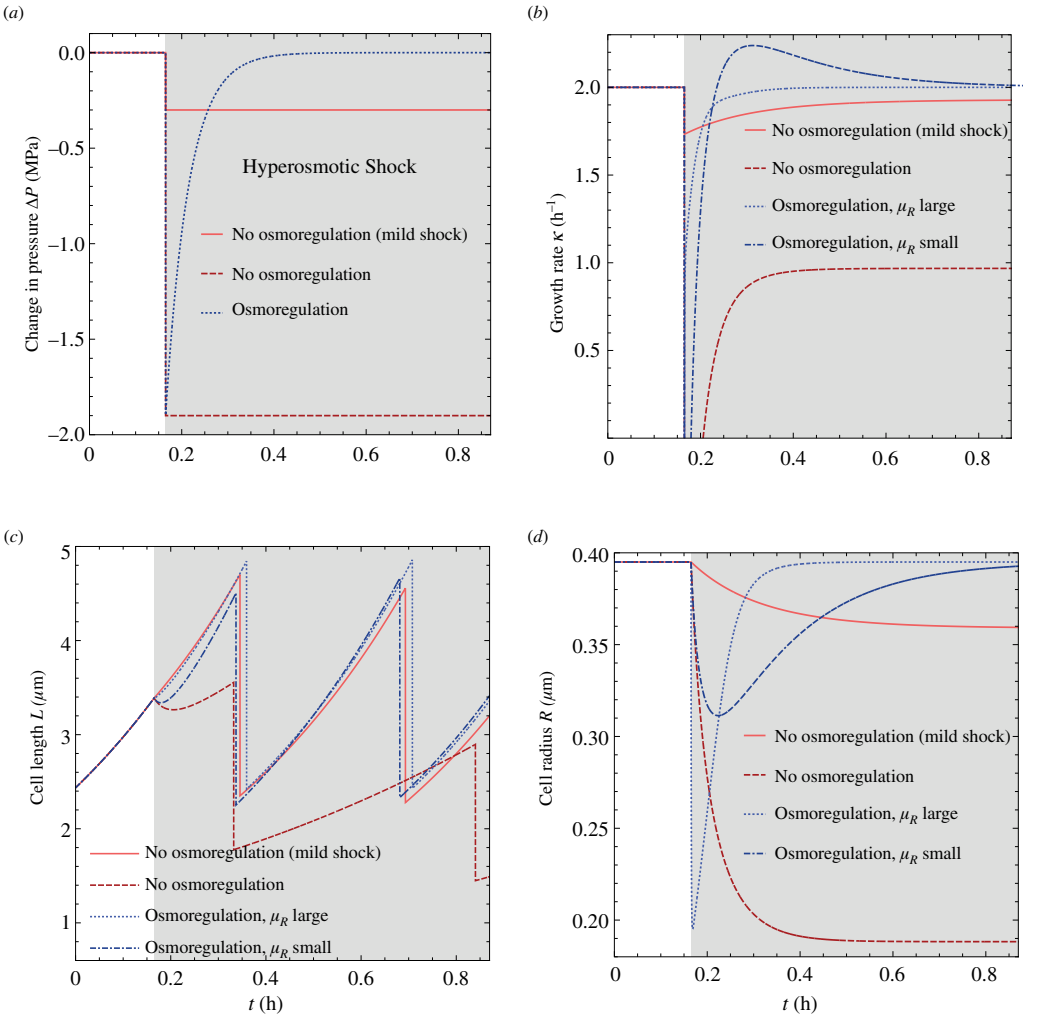

Figure 7. Adaptation to hyperosmotic shocks. (*a*) Change in turgor pressure ($\Delta P = P_0 - P_f$) versus time plots under a hyperosmotic shock. The white region indicates the pre-shock period and the grey region indicates the post-shock environment. Osmoregulation is modelled here as an exponential relaxation of turgor pressure back to the pre-shock pressure $P_0 = 0.3$ MPa with a decay constant $\tau_p^{-1} = 20$ h^{-1}. (*b*) Growth rate versus time plots of corresponding to the pressure perturbations in panel (*a*). (*c*) Representative cell length trajectories corresponding to the pressure perturbations in panel (*a*). (*d*) Cell radius versus time plots corresponding to the pressure perturbations in panel (*a*).

$-PV$ for large values of the final turgor pressure P_f. In other words, the cost of increased cell size can outweigh the minimization of energy from relieving pressure in the model. Even when pressure naturally relaxes due to volume changes and osmoregulation (figure 8*a*), the observed behaviour resembles that of a hyperosmotic shock, with an initial sharp decline in growth rate and cell size followed by an overshoot in growth rate to the new steady-state (figure 8*b–d*). The value of P_f chosen for these simulations is large enough that the growth rate stabilizes to a negative value, indicating an unstable state within our model where the cell would either die or the optimal growth flux assumption is no longer valid.

To more realistically model cellular response to hypoosmotic shocks within our theoretical framework, we need to consider potential changes in the mechanical properties of the cell wall. Recent work has both measured and modelled the softening of the cell wall in response to hyperosmotic shocks [68]. This prompts us to explore alterations in cellular strain energy under

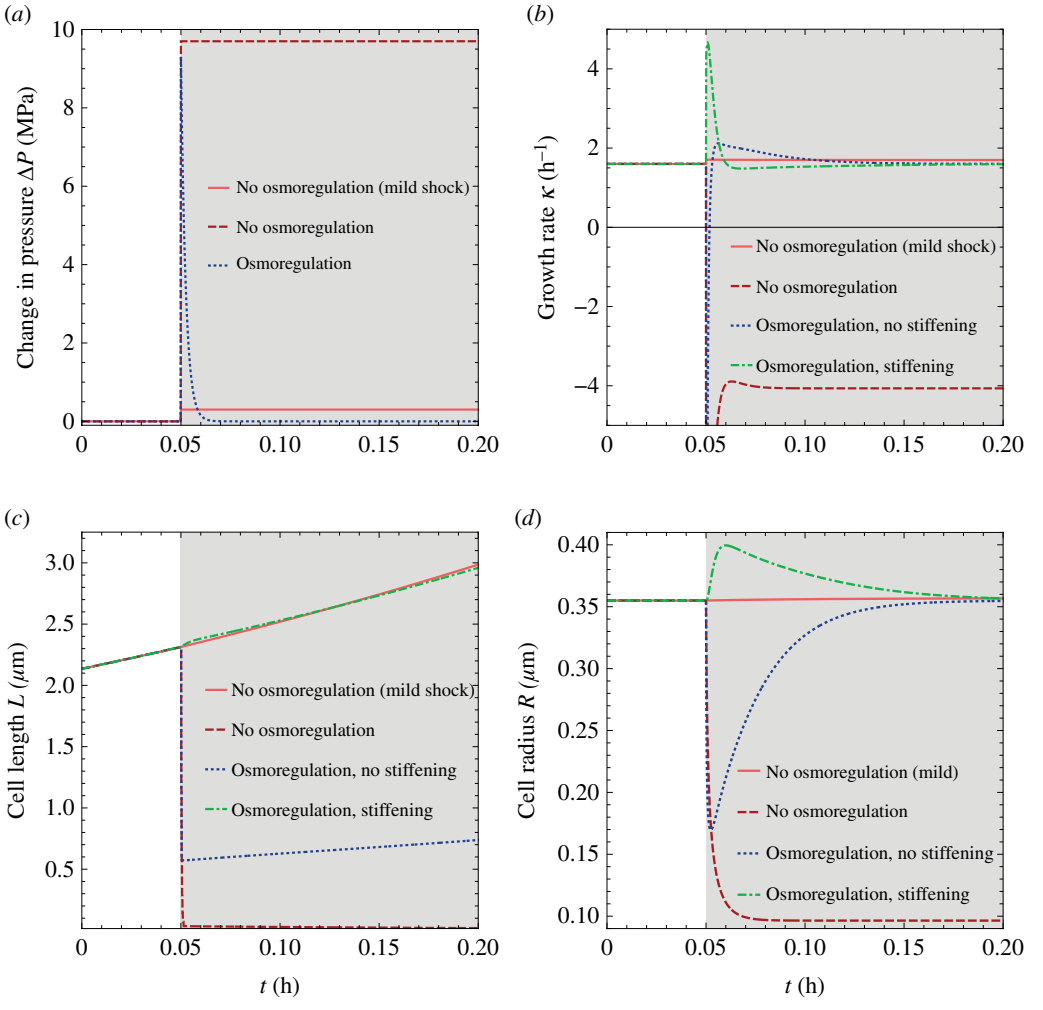

Figure 8. Adaptation to hypoosmotic shocks. (*a*) Change in turgor pressure (ΔP) versus time plots for a bacterial cell under a hypoosmotic shock. The white region indicates the pre-shock period and the grey region indicates the post-shock environment. Osmoregulation is modelled here as exponential decay of the post-shock turgor pressure back to the pre-shock pressure $P_0 = 0.3$ MPa with a decay constant $\tau_p^{-1} = 400$ h^{-1}. Temporary stiffening of the cell envelope is also modelled as exponential decay from the perturbed value $\lambda/P^2 = 0.23$ MPa^{-1}h^{-1} back to the pre-shock value with a decay constant 50 h^{-1}. (*b*) Growth rate versus time plots corresponding to the pressure perturbations in panel (*a*). (*c*) Representative cell length trajectories corresponding to the pressure perturbations in panel (*a*). (*d*) Cell radius versus time plots corresponding to the pressure perturbations in panel (*a*).

hypoosmotic shocks, which is governed by the parameter $\lambda = P^2\rho_g/4k_s\rho_p$ (see 2.4). In contrast to hyperosmotic shocks, if the cell envelope stiffens under hypoosmotic shock (increased k_s) as it is stretched beyond the usual regime, λ would be expected to temporarily decrease. This decrease in λ could also result from a reduction in the glycan strand density (ρ_g) as the cell temporarily swells at a greater rate than the synthesis of glycan strands.

We thus dynamically increased cell-wall stiffness k_s during a hypoosmotic shock, using the same exponential relaxation form as in equation (5.1), with an independent decay constant. As shown in figure 8*a–d*, incorporating such a temporary increase in stiffness k_s simultaneously with the increase in P results in the initial swelling of the cell as expected. This is followed

by a relaxation of growth rate and cell sizes to a similar value as the pre-shock rate, with the potential for an undershoot in growth rate depending on μ_R. The value of P_f chosen for this figure generates growth-rate trajectories that resemble the scale of the experimental data [24], indicating that the pressures required for the osmoregulation model to match data would not be stable growth conditions for non-osmoregulating cells. We thus predict that a temporary stiffening of the cell wall is essential to capture the experimentally observed growth rate dynamics [24] in response to a hypoosmotic shock. This prediction could be tested in future experiments.

6. Discussion

All living organisms rely on energy assimilation and the efficient allocation of acquired energy to perform various physiological tasks. While theoretical models connecting energy, metabolism and growth have been developed for birds and mammals [1–5], understanding energy allocation strategies in microorganisms has remained an open problem. In this paper, we address this gap by developing a theoretical framework for energy allocation in growing bacterial cells based on optimizing the rate of energy used for growth. We partition the use of imported energy into cellular metabolism and energy storage, with the former further divided into energy for growth, division, shape maintenance and dissipation. Optimizing the energy flux to maximize growth results in equations of motion for cell size and protein production, predicting an increase in cell size with growth rate. While most of the model parameters can be directly estimated from published data on *E. coli*, a few are calibrated from experimental conditions or are determined by fitting the model to perturbation experiments.

Analysing the energy dynamics throughout a cell cycle, we observe that the rate at which each energy sector accumulates energy is directly proportional to cell size. Across various growth environments, the fraction of energy utilized for mechanical tasks exhibits a minimum at a preferred cell size, while growth energy and dissipation increase with nutrient quality, trading off with stored energy and division. Notably, the fraction of energy allocated to growth increases with growth rate, consistent with the observation that the ribosome mass fraction also increases with growth rate [11].

An important implication of our theory is that it provides a rationale for the nonlinear increase in metabolic rate with cell size in bacteria [65]. Without incorporating additional regulatory mechanisms, our model predicts a superlinear scaling of metabolic rate with cell size, with a tunable scaling exponent determined by changes in stored energy density g. This superlinear metabolic scaling arises from the increase in cell size with growth rate. If cell size were independent of growth rate, a linear scaling of metabolic rate with cell size would be expected. Conversely, a decrease in growth rate with size would result in sublinear metabolic scaling.

Given the dynamic formulation of our model, it is well suited to capture cellular behaviours out of steady state, such as during nutrient shifts. We find that our postulate of growth energy flux optimization is capable of capturing these transient dynamics. In nutrient upshifts, we find that nutrient import and cell size both steadily increase together during the shift, whereas in nutrient downshifts we can capture the observed undershoot in growth rate due to nutrient importation decreasing on a faster timescale than cell size.

The predicted behaviours of our model for nutrient shifts align with proteome partitioning models, where changes in growth rate are driven by shifts in proteome allocation, translation rate and amino acid precursor levels [17,20,49]. A valuable comparison can be drawn between the energy allocation framework and proteome allocation models. In the latter, dynamics of proteome reallocation aim to maximize growth rate in the new environment, akin to our model where energy reallocation is dictated by the maximization of energy flux for growth, directly proportional to the growth rate. Although we do not explicitly model the allocation

of ribosomal proteins that increases with nutrient quality, the increase in energy allocation to growth could be interpreted as originating from an increased mass fraction of ribosomal protein sector. Furthermore, the decrease in energy allocation to the division sector with growth rate is consistent with a reduced allocation to the division protein sector in proteome-centric models [20,37]. The increase in nutrient import with growth rate corresponds to an elevated flux of amino acid precursors, resulting in a higher amino acid mass fraction during faster growth. From a proteome theory perspective, the observed growth rate undershoots in nutrient downshifts may be explained by a temporary undershoot in the amino acid mass fraction, as precursors are depleted faster than they are imported. This interpretation aligns with our model, where nutrient import decreases rapidly while cell size and associated energy costs lag behind.

One of the advantages of using the energy-based model as opposed to a proteome partitioning theory is that we can investigate the cellular response to mechanical perturbations without adding any new components to the model. By perturbing the turgor pressure, we can effectively capture the cellular response to hyperosmotic shocks with partial growth rate recovery and capture complete recovery if osmoregulation is taken into account. We find that osmoregulation is necessary to model hypoosmotic shocks, as well as changes to the mechanical properties of the cell wall. Recent work has elucidated that Gram-positive cells employ a feedback loop to sustain growth homeostasis following osmotic shocks [67]. As pressure changes cause expansion or contraction of the cell wall, altering membrane tension, this tension inversely influences precursor flux, thereby regulating growth rate to maintain homeostasis between wall and membrane synthesis. Although our model inherently includes feedback between mechanical stress, growth and cell size, we currently lack feedback between nutrient import and mechanical stress in the cell envelope. To accurately model osmotic shock behaviour in Gram-positive cells, it might be essential to integrate such a feedback system into our model.

Beyond addressing the cellular response to nutrient or osmotic stresses, our model holds the potential to investigate various environmental perturbations, including temperature changes [71] and stresses induced by antibiotics affecting cell growth and cell envelope properties [72–75]. Permitting gradual adaptation of calibrated biophysical parameters to simulate changes in genotype could allow for exploration of long-term behaviour. The theory is not constrained by the shape of the cells [22] and the equations of motion can be easily developed for spherical or curved bacteria as well as cells with non-uniform shapes. This adaptability enables the application of the model to a diverse array of cell morphologies, such as flattened bacteria experiencing mechanical stress [76]. Moreover, recent experimental findings [77] revealing non-monotonic changes in ATP concentration between cell birth and division suggest a promising avenue for refining our understanding of energy utilization throughout the cell cycle by establishing connections between metabolic energy and ATP production.

Data accessibility. Data and codes that support the findings of this study are available at Zenodo [78].

Declaration of AI use. We have not used AI-assisted technologies in creating this article.

Authors' contributions. A.C.: conceptualization, formal analysis, methodology, validation, visualization, writing—original draft, writing—review and editing; D.S.: conceptualization, formal analysis, methodology, visualization, writing—original draft; S.B.: conceptualization, validation, visualization, funding acquisition, methodology, project administration, supervision, writing—original draft, writing—review and editing.

All authors gave final approval for publication and agreed to be held accountable for the work performed therein.

Conflict of interest declaration. We declare that we have no competing interests.

Funding. S.B. acknowledges support from the Royal Society (RGF/EA/181044), the National Institutes of Health (NIH R35 GM143042), and the Shurl and Kay Curci Foundation.

Acknowledgements. S.B. and A.C. acknowledge support from the Department of Physics at Carnegie Mellon University.

References

1. Brody S, Lardy HA. 1946 Bioenergetics and growth. *J. Phys. Chem.* **50**, 168–169. (doi:10.1021/j150446a008)
2. Kleiber M. 1961 *The fire of life. An introduction to animal energetics*. New York, NY: John Wiley & Sons, Inc.
3. Kooijman S. 2000 *Dynamic energy and mass budgets in biological systems*. Cambridge, UK: Cambridge University Press.
4. West GB, Brown JH, Enquist BJ. 2001 A general model for ontogenetic growth. *Nature* **413**, 628–631. (doi:10.1038/35098076)
5. Hou C, Zuo W, Moses ME, Woodruff WH, Brown JH, West GB. 2008 Energy uptake and allocation during ontogeny. *Science* **322**, 736–739. (doi:10.1126/science.1162302)
6. Goyal A, Flamholz AI, Petroff AP, Murugan A. 2023 Closed ecosystems extract energy through self-organized nutrient cycles. *Proc. Natl Acad. Sci. USA* **120**. (doi:10.1073/pnas.2309387120)
7. Baldazzi V, Ropers D, Gouzé JL, Gedeon T, de Jong H. 2023 Resource allocation accounts for the large variability of rate-yield phenotypes across bacterial strains. *Elife* **12**, e79815. (doi:10.7554/eLife.79815)
8. Pirt SJ. 1965 The maintenance energy of bacteria in growing cultures. *Proc. R. Soc. Lond. B Biol. Sci.* **163**, 224–231. (doi:10.1098/rspb.1965.0069)
9. Kempes CP, Dutkiewicz S, Follows MJ. 2012 Growth, metabolic partitioning, and the size of microorganisms. *Proc. Natl Acad. Sci. USA* **109**, 495–500. (doi:10.1073/pnas.1115585109)
10. Jun S, Si F, Pugatch R, Scott M. 2018 Fundamental principles in bacterial physiology-history, recent progress, and the future with focus on cell size control: a review. *Rep. Prog. Phys.* **81**, 056601. (doi:10.1088/1361-6633/aaa628)
11. Scott M, Gunderson CW, Mateescu EM, Zhang Z, Hwa T. 2010 Interdependence of cell growth and gene expression: origins and consequences. *Science* **330**, 1099–1102. (doi:10.1126/science.1192588)
12. Scott M, Klumpp S, Mateescu EM, Hwa T. 2014 Emergence of robust growth laws from optimal regulation of ribosome synthesis. *Mol. Syst. Biol.* **10**, 747. (doi:10.15252/msb.20145379)
13. Hui S, Silverman JM, Chen SS, Erickson DW, Basan M, Wang J, Hwa T, Williamson JR. 2015 Quantitative proteomic analysis reveals a simple strategy of global resource allocation in bacteria. *Mol. Syst. Biol.* **11**, 784. (doi:10.15252/msb.20145697)
14. Weiße AY, Oyarzún DA, Danos V, Swain PS. 2015 Mechanistic links between cellular trade-offs, gene expression, and growth. *Proc. Natl Acad. Sci. USA* **112**, E1038–47. (doi:10.1073/pnas.1416533112)
15. Serbanescu D, Ojkic N, Banerjee S. 2022 Cellular resource allocation strategies for cell size and shape control in bacteria. *FEBS J.* **289**, 7891–7906. (doi:10.1111/febs.16234)
16. Giordano N, Mairet F, Gouzé JL, Geiselmann J, de Jong H. 2016 Dynamical allocation of cellular resources as an optimal control problem: novel insights into microbial growth strategies. *PLoS Comput. Biol.* **12**, e1004802. (doi:10.1371/journal.pcbi.1004802)
17. Erickson DW, Schink SJ, Patsalo V, Williamson JR, Gerland U, Hwa T. 2017 A global resource allocation strategy governs growth transition kinetics of *Escherichia coli*. *Nature* **551**, 119–123. (doi:10.1038/nature24299)
18. Mori M, Schink S, Erickson DW, Gerland U, Hwa T. 2017 Quantifying the benefit of a proteome reserve in fluctuating environments. *Nat. Commun.* **8**, 1225. (doi:10.1038/s41467-017-01242-8)
19. Korem Kohanim Y, Levi D, Jona G, Towbin BD, Bren A, Alon U. 2018 A bacterial growth law out of steady state. *Cell Rep.* **23**, 2891–2900. (doi:10.1016/j.celrep.2018.05.007)
20. Kratz JC, Banerjee S. 2023 Dynamic proteome trade-offs regulate bacterial cell size and growth in fluctuating nutrient environments. *Commun. Biol.* **6**, 486. (doi:10.1038/s42003-023-04865-4)
21. Jiang H, Sun SX. 2010 Morphology, growth, and size limit of bacterial cells. *Phys. Rev. Lett.* **105**, 028101. (doi:10.1103/PhysRevLett.105.028101)

22. Banerjee S, Scherer NF, Dinner AR. 2016 Shape dynamics of growing cell walls. *Soft Matter* **12**, 3442–3450. (doi:10.1039/c5sm02991k)
23. Panlilio M, Grilli J, Tallarico G, Iuliani I, Sclavi B, Cicuta P, Cosentino Lagomarsino M. 2021 Threshold accumulation of a constitutive protein explains *E. coli* cell-division behavior in nutrient upshifts. *Proc. Natl Acad. Sci. USA* **118**, e2016391118. (doi:10.1073/pnas.2016391118)
24. Rojas E, Theriot JA, Huang KC. 2014 Response of *Escherichia coli* growth rate to osmotic shock. *Proc. Natl Acad. Sci. USA* **111**, 7807–7812. (doi:10.1073/pnas.1402591111)
25. Belliveau NM, Chure G, Hueschen CL, Garcia HG, Kondev J, Fisher DS, Theriot JA, Phillips R. 2021 Fundamental limits on the rate of bacterial growth and their influence on proteomic composition. *Cell Syst.* **12**, 924–944.(doi:10.1016/j.cels.2021.06.002)
26. Mahone CR, Goley ED. 2020 Bacterial cell division at a glance. *J. Cell. Sci.* **133**, jcs237057. (doi:10.1242/jcs.237057)
27. Osawa M, Anderson DE, Erickson HP. 2009 Curved FtsZ protofilaments generate bending forces on liposome membranes. *EMBO J.* **28**, 3476–3484. (doi:10.1038/emboj.2009.277)
28. Erickson HP, Anderson DE, Osawa M. 2010 FtsZ in bacterial cytokinesis: cytoskeleton and force generator all in one. *Microbiol. Mol. Biol. Rev.* **74**, 504–528. (doi:10.1128/MMBR.00021-10)
29. Typas A, Banzhaf M, Gross CA, Vollmer W. 2012 From the regulation of peptidoglycan synthesis to bacterial growth and morphology. *Nat. Rev. Microbiol.* **10**, 123–136. (doi:10.1038/nrmicro2677)
30. Lan G, Wolgemuth CW, Sun SX. 2007 Z-ring force and cell shape during division in rod-like bacteria. *Proc. Natl Acad. Sci. USA* **104**, 16110–16115. (doi:10.1073/pnas.0702925104)
31. Allard JF, Cytrynbaum EN. 2009 Force generation by a dynamic Z-ring in *Escherichia coli* cell division. *Proc. Natl Acad. Sci. USA* **106**, 145–150. (doi:10.1073/pnas.0808657106)
32. Reshes G, Vanounou S, Fishov I, Feingold M. 2008 Cell shape dynamics in *Escherichia coli*. *Biophys. J.* **94**, 251–264. (doi:10.1529/biophysj.107.104398)
33. Banerjee S, Lo K, Daddysman MK, Selewa A, Kuntz T, Dinner AR, Scherer NF. 2017 Biphasic growth dynamics control cell division in *Caulobacter crescentus*. *Nat. Microbiol.* **2**, 17116. (doi:10.1038/nmicrobiol.2017.116)
34. Taheri-Araghi S, Bradde S, Sauls JT, Hill NS, Levin PA, Paulsson J, Vergassola M, Jun S. 2015 Cell-size control and homeostasis in bacteria. *Curr. Biol.* **25**, 385–391. (doi:10.1016/j.cub.2014.12.009)
35. Ghusinga KR, Vargas-Garcia CA, Singh A. 2016 A mechanistic stochastic framework for regulating bacterial cell division. *Sci. Rep.* **6**, 30229. (doi:10.1038/srep30229)
36. Si F, Le Treut G, Sauls JT, Vadia S, Levin PA, Jun S. 2019 Mechanistic origin of cell-size control and homeostasis in bacteria. *Curr. Biol.* **29**, 1760–1770.(doi:10.1016/j.cub.2019.04.062)
37. Serbanescu D, Ojkic N, Banerjee S. 2020 Nutrient-dependent trade-offs between ribosomes and division protein synthesis control bacterial cell size and growth. *Cell Rep.* **32**, 108183. (doi:10.1016/j.celrep.2020.108183)
38. Ojkic N, Serbanescu D, Banerjee S. 2019 Surface-to-volume scaling and aspect ratio preservation in rod-shaped bacteria. *eLife* **8**, e47033. (doi:10.7554/eLife.47033)
39. von Stockar U, Liu JS. 1999 Does microbial life always feed on negative entropy? Thermodynamic analysis of microbial growth. *Biochim. et Biophys. Acta (BBA) - Bioenerg.* **1412**, 191–211. (doi:10.1016/S0005-2728(99)00065-1)
40. Onsager L. 1931 Reciprocal relations in irreversible processes. I. *Phys. Rev.* **37**, 405–426. (doi:10.1103/PhysRev.37.405)
41. Doi M. 2011 Onsager's variational principle in soft matter. *J. Phys. Condens. Matter* **23**, 284118. (doi:10.1088/0953-8984/23/28/284118)
42. Groot SR, Mazur P. 2013 *Non-equilibrium thermodynamics*. New York, NY: Dover Publications.
43. Odum HT. 1983 Maximum power and efficiency: a rebutttal. *Ecol. Modell.* **20**, 71–82. (doi:10.1016/0304-3800(83)90032-7)
44. Brown MT, Odum HT, Jorgensen SE. 2004 Energy hierarchy and transformity in the universe. *Ecol. Modell.* **178**, 17–28. (doi:10.1016/j.ecolmodel.2003.12.002)
45. Edwards JS, Ibarra RU, Palsson BO. 2001 *In silico* predictions of *Escherichia coli* metabolic capabilities are consistent with experimental data. *Nat. Biotechnol.* **19**, 125–130. (doi:10.1038/84379)

46. Ibarra RU, Edwards JS, Palsson BO. 2002 *Escherichia coli* K-12 undergoes adaptive evolution to achieve *in silico* predicted optimal growth. *Nature* **420**, 186–189. (doi:10.1038/nature01149)
47. Lewis NE *et al.* 2010 Omic data from evolved *E. coli* are consistent with computed optimal growth from genome-scale models. *Mol. Syst. Biol.* **6**, 390. (doi:10.1038/msb.2010.47)
48. Bosdriesz E, Molenaar D, Teusink B, Bruggeman FJ. 2015 How fast-growing bacteria robustly tune their ribosome concentration to approximate growth-rate maximization. *FEBS J.* **282**, 2029–2044. (doi:10.1111/febs.13258)
49. Molenaar D, van Berlo R, de Ridder D, Teusink B. 2009 Shifts in growth strategies reflect tradeoffs in cellular economics. *Mol. Syst. Biol.* **5**, 323. (doi:10.1038/msb.2009.82)
50. Pandey PP, Jain S. 2016 Analytic derivation of bacterial growth laws from a simple model of intracellular chemical dynamics. *Theory Biosci.* **135**, 121–130. (doi:10.1007/s12064-016-0227-9)
51. Schink S, Ammar C, Chang YF, Zimmer R, Basan M. 2022 Analysis of proteome adaptation reveals a key role of the bacterial envelope in starvation survival. *Mol. Syst. Biol.* **18**, e11160. (doi:10.15252/msb.202211160)
52. Balakrishnan R, Cremer J. 2023 Conditionally unutilized proteins and their profound effects on growth and adaptation across microbial species. *Curr. Opin. Microbiol.* **75**, 102366. (doi:10.1016/j.mib.2023.102366)
53. Si F *et al.* 2017 Invariance of initiation mass and predictability of cell size in *Escherichia coli*. *Curr. Biol.* **27**, 1278–1287. (doi:10.1016/j.cub.2017.03.022)
54. Hussain S *et al.* 2018 MreB filaments align along greatest principal membrane curvature to orient cell wall synthesis. *Elife* **7**, e32471. (doi:10.7554/eLife.32471)
55. Rueda S, Vicente M, Mingorance J. 2003 Concentration and assembly of the division ring proteins FtsZ, FtsA, and ZipA during the *Escherichia coli* cell cycle. *J. Bacteriol.* **185**, 3344–3351. (doi:10.1128/JB.185.11.3344-3351.2003)
56. Misra G, Rojas ER, Gopinathan A, Huang KC. 2013 Mechanical consequences of cell-wall turnover in the elongation of a Gram-positive bacterium. *Biophys. J.* **104**, 2342–2352. (doi:10.1016/j.bpj.2013.04.047)
57. Belgrave AMT, Wolgemuth CW. 2013 Elasticity and biochemistry of growth relate replication rate to cell length and cross-link density in rod-shaped bacteria. *Biophys. J.* **104**, 2607–2611. (doi:10.1016/j.bpj.2013.04.028)
58. Phillips R, Milo R. 2009 A feeling for the numbers in biology. *Proc. Natl Acad. Sci. USA* **106**, 21465–21471. (doi:10.1073/pnas.0907732106)
59. Anderson DE, Gueiros-Filho FJ, Erickson HP. 2004 Assembly dynamics of FtsZ rings in *Bacillus subtilis* and *Escherichia coli* and effects of FtsZ-regulating proteins. *J. Bacteriol.* **186**, 5775–5781. (doi:10.1128/JB.186.17.5775-5781.2004)
60. Basan M, Hui S, Okano H, Zhang Z, Shen Y, Williamson JR, Hwa T. 2015 Overflow metabolism in *Escherichia coli* results from efficient proteome allocation. *Nature* **528**, 99–104. (doi:10.1038/nature15765)
61. Bertaux F, von Kügelgen J, Marguerat S, Shahrezaei V. 2020 A bacterial size law revealed by a coarse-grained model of cell physiology. *PLoS Comput. Biol.* **16**, e1008245. (doi:10.1371/journal.pcbi.1008245)
62. Schmidt A *et al.* 2016 The quantitative and condition-dependent *Escherichia coli* proteome. *Nat. Biotechnol.* **34**, 104–110. (doi:10.1038/nbt.3418)
63. Mori M *et al.* 2021 From coarse to fine: the absolute *Escherichia coli* proteome under diverse growth conditions. *Mol. Syst. Biol.* **17**, e9536. (doi:10.15252/msb.20209536)
64. Kleiber M. 1932 Body size and metabolism. *Hilg.* **6**, 315–353. (doi:10.3733/hilg.v06n11p315)
65. DeLong JP, Okie JG, Moses ME, Sibly RM, Brown JH. 2010 Shifts in metabolic scaling, production, and efficiency across major evolutionary transitions of life. *Proc. Natl Acad. Sci. USA* **107**, 12941–12945. (doi:10.1073/pnas.1007783107)
66. Marshall DJ, Malerba M, Lines T, Sezmis AL, Hasan CM, Lenski RE, McDonald MJ. 2022 Long-term experimental evolution decouples size and production costs in *Escherichia coli*. *Proc. Natl Acad. Sci. USA* **119**, e2200713119. (doi:10.1073/pnas.2200713119)
67. Rojas ER, Huang KC, Theriot JA. 2017 Homeostatic cell growth is accomplished mechanically through membrane tension inhibition of cell-wall synthesis. *Cell Syst.* **5**, 578–590.(doi:10.1016/j.cels.2017.11.005)

68. Al-Mosleh S, Gopinathan A, Santangelo CD, Huang KC, Rojas ER. 2022 Feedback linking cell envelope stiffness, curvature, and synthesis enables robust rod-shaped bacterial growth. *Proc. Natl Acad. Sci. USA* **119**, e2200728119. (doi:10.1073/pnas.2200728119)
69. Wood JM. 2015 Perspectives on: the response to osmotic challenges: bacterial responses to osmotic challenges. *J. Gen. Physiol.* **145**, 381. (doi:10.1085/jgp.201411296)
70. Rojas ER, Huang KC. 2018 Regulation of microbial growth by turgor pressure. *Curr. Opin. Microbiol.* **42**, 62–70. (doi:10.1016/j.mib.2017.10.015)
71. Kumar P, Libchaber A. 2013 Pressure and temperature dependence of growth and morphology of *Escherichia coli*: experiments and stochastic model. *Biophys. J.* **105**, 783–793. (doi:10.1016/j.bpj.2013.06.029)
72. Yao Z, Kahne D, Kishony R. 2012 Distinct single-cell morphological dynamics under beta-lactam antibiotics. *Mol. Cell* **48**, 705–712. (doi:10.1016/j.molcel.2012.09.016)
73. Banerjee S, Lo K, Ojkic N, Stephens R, Scherer NF, Dinner AR. 2021 Mechanical feedback promotes bacterial adaptation to antibiotics. *Nat. Phys.* **17**, 403–409. (doi:10.1038/s41567-020-01079-x)
74. Ojkic N, Serbanescu D, Banerjee S. 2022 Antibiotic resistance via bacterial cell shape-shifting. *mBio* **13**, e0065922. (doi:10.1128/mbio.00659-22)
75. Cylke C, Si F, Banerjee S. 2022 Effects of antibiotics on bacterial cell morphology and their physiological origins. *Biochem. Soc. Trans.* **50**, 1269–1279. (doi:10.1042/BST20210894)
76. Si F, Li B, Margolin W, Sun SX. 2015 Bacterial growth and form under mechanical compression. *Sci. Rep.* **5**, 11367. (doi:10.1038/srep11367)
77. Lin WH, Jacobs-Wagner C. 2022 Connecting single-cell ATP dynamics to overflow metabolism, cell growth, and the cell cycle in *Escherichia coli*. *Curr. Biol.* **32**, 3911–3924.(doi: 10.1016/j.cub.2022.07.035)
78. Cylke A, Banerjee S. BanerjeeLab/Energy_allocation_theory: EAT Version 1.0. Zenodo (doi: 10.5281/zenodo.13369891)